Nanoscale
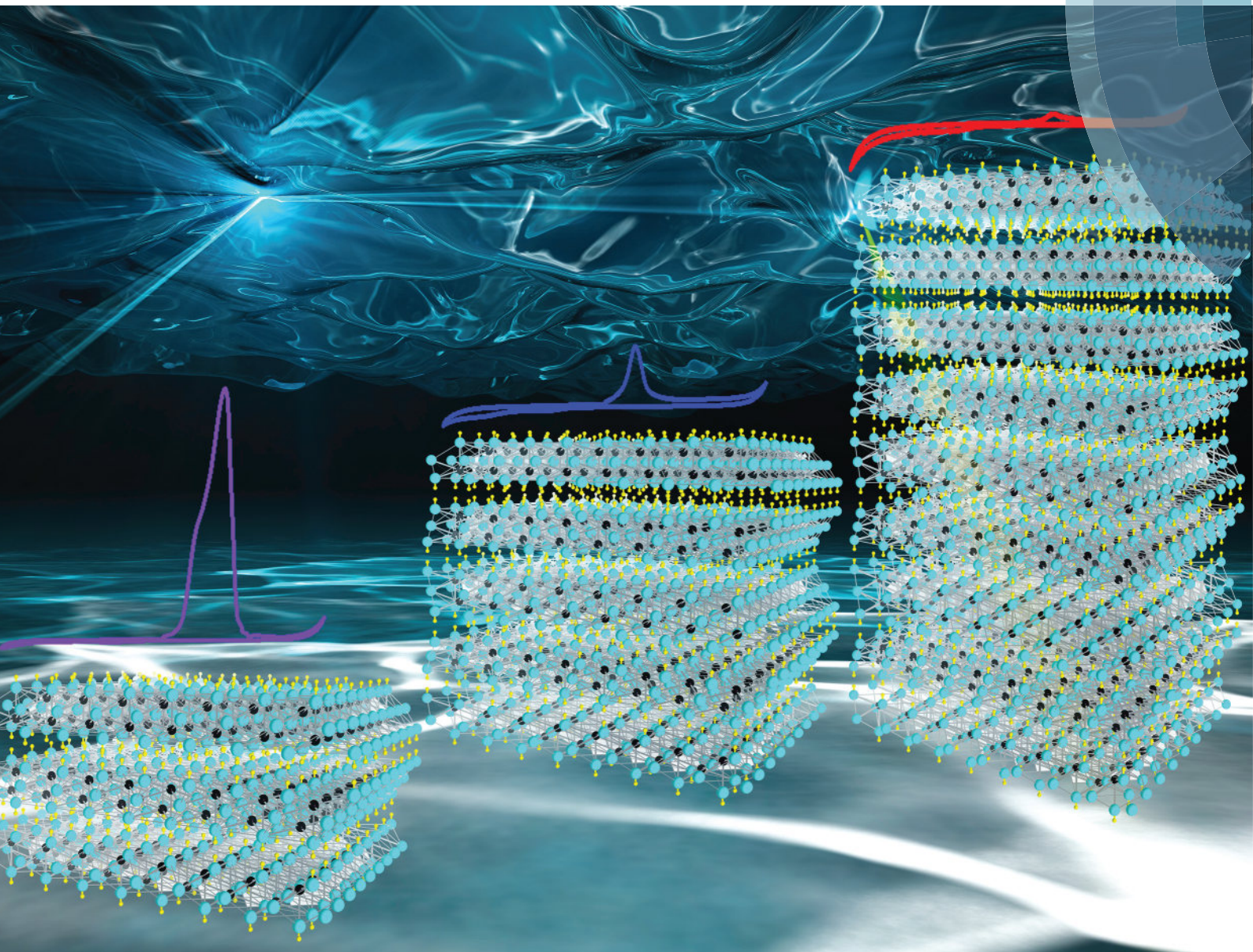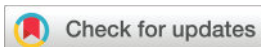
ROYAL SOCIETY
OF CHEMISTRY

PAPER
Husam N. Alshareef *et al.*
Inherent electrochemistry and charge transfer properties of few-layered
two-dimensional Ti$_3$C$_2$T$_x$ MXene

NCNST

Nanoscale

Inherent electrochemistry and charge transfer properties of few-layered two-dimensional $Ti_3C_2T_x$ MXene†

Pranati Nayak,‡[a,b] Qiu Jiang,‡[a] Rajeshkumar Mohanraman,‡[a] Dalaver Anjum,[c] Mohamed Nejib Hedhili[c] and Husam N. Alshareef [ID] *[a]

We report the effect of the $Ti_3C_2T_x$ MXene flake thickness on its inherent electrochemistry and heterogeneous charge transfer characteristics. It is shown that $Ti_3C_2T_x$ undergoes irreversible oxidation in a positive potential window, which strongly depends on the flake thickness and pH of the electrolyte. Few-layered $Ti_3C_2T_x$ exhibits faster electron transfer kinetics (k^0 = 0.09533 cm s^{-1}) with a $[Fe(CN)_6]^{4-/3-}$ redox mediator compared to multi-layered $Ti_3C_2T_x$ (k^0 = 0.00503 cm s^{-1}). In addition, the few-layered free standing $Ti_3C_2T_x$ film electrode remains intact after enduring irreversible oxidation.

Introduction

Successful isolation of graphene and realization of its remarkable electronic, mechanical, thermal, optical, and electrochemical properties spurred the investigation of the fundamental properties of other two-dimensional (2D) materials. Amidst, a new family of 2D materials known as MXenes, was discovered in 2011.[1] Allied with a layered graphitic structure, MXenes are stacks of 2D early transition metal carbides, nitrides and carbonitrides of the general formula $M_{n+1}X_nT_x$, where M stands for a metal atom, X stands for C and/or N, n = 1, 2, or 3, and T_x represents various surface terminations (–OH, –O, and/or –F groups).[2] MXenes are composed of a conductive carbon core with an outer transition metal oxide/hydroxide like surface produced by selective etching of the A layers from ternary $M_{n+1}AX_n$ phases, where A is mainly a group IIIA or IVA (*i.e.*, group 13 or 14) element. The atoms are held together by strong mixed covalent/metallic/ionic bonds within the layers, whereas stacked layers after "A" removal are weakly bonded with hydrogen bonds.[3]

The past few years have witnessed an exponential increase in research on 2D MXenes, which has elucidated many of its promising properties such as hydrophilicity, good mechanical strength, and superior ion interaction capacity.[4,5] The unique combination of excellent metallic conductivity with solution processability could potentially make MXene as an outstanding electrode material for many applications such as electrochemical capacitors, mobile ion batteries, and electromagnetic interference shielding.[6,7] Though relatively new to many other fields, some members of the MXene family have also been studied for their electronic properties, energy harvesting and storage device fabrication.[8,9] Among the MXenes, $Ti_3C_2T_x$ MXene has been well investigated and etching recipes were optimized to control the quality of MXene layers. Recently, it has been shown that $Ti_3C_2T_x$ MXene exhibits proton induced pseudocapacitance in acidic electrolytes, which can be attributed to the reversible redox reactions of the transition metal in non-aqueous medium.[10] However, there is limited understanding of the inherent electrochemistry of $Ti_3C_2T_x$ MXene in aqueous solutions, *i.e.* how $Ti_3C_2T_x$ MXenes behave under oxidative/reductive potential irrespective of the analyte in the aqueous solution. Many electrochemical applications such as a biosensor, a chemical sensor, and catalysis require catalytic properties and good stability of the electrode material in an aqueous solution of different pH.

Herein, we report a systematic investigation of the inherent electrochemistry and heterogeneous electron transfer (HET) characteristics of few and multi-layered $Ti_3C_2T_x$ MXene, leading to important conclusions for the use of $Ti_3C_2T_x$ MXene in various electrochemical applications in aqueous medium. Our study shows that the $Ti_3C_2T_x$ MXene exhibits strong inherent electrochemical properties, which are enhanced

[a]*Materials Science and Engineering, Physical Sciences & Engineering Division, King Abdullah University of Science and Technology (KAUST), Thuwal 23955-6900, Saudi Arabia. E-mail: husam.alshareef@kaust.edu.sa*
[b]*Electrodics and Electrocatalysis (EEC) Biosensor Division, CSIR-Central Electrochemical Research Institute (CSIR-CECRI), Karaikudi, Tamilnadu, 630006, India*
[c]*Core Labs, King Abdullah University of Science and Technology (KAUST), Thuwal 23955-6900, Saudi Arabia*
†Electronic supplementary information (ESI) available. See DOI: 10.1039/c8nr01883a
‡Contributed equally.

when multi-layered MXene is sliced to few-layered flakes. This behavior possibly stems from the more accessible electrochemical surface area in the few-layered flakes of $Ti_3C_2T_x$.[11] Such a large surface area in delaminated few-layered flakes carries defects and a high density of edge plane sites, which are potentially active sites for electrochemical sensing and energy-related applications.[12]

Results and discussion

The MXenes reported in this study were prepared by selective etching of the Al layer from the Ti_3AlC_2 MAX phase. The detailed synthesis protocol is outlined in Scheme 1. The characterization of parent MAX phase and $Ti_3C_2T_x$ MXene is discussed in the ESI, Fig. S1.† The $Ti_3C_2T_x$ MXene consists of 2D $Ti_3C_2T_x$ layers stacked in a 3D bulk form with large interlayer spacing due to the removal of the 'Al' lattice plane from the parent Ti_3AlC_2 MAX phase and hereafter will be named bulk-$Ti_3C_2T_x$ for our convenience. We attempted to decrease the layer thickness of bulk-$Ti_3C_2T_x$ by a simple clay method followed by ultrasonication (multi-layered MXene, ML-$Ti_3C_2T_x$) and minimum intensive layer delamination root (MILD method, few-layered MXene, FL-$Ti_3C_2T_x$).[13,14] Unlike the parent MAX phase, the bulk-$Ti_3C_2T_x$ consists of a stack of a large number of 2D layers as shown in the FESEM and high-resolution transmission electron microscopy (HRTEM) images in Fig. S1.† It is clear that larger and thinner MXene flakes can be achieved using the MILD method (Fig. 1a) compared to the clay method (Fig. 1b). The AFM images (Fig. 1c), corresponding height profiles (Fig. S2a†), and the statistical distribution of the thickness (Fig. 1e) show significantly thinner flakes (1 nm to ~2 nm thick), which indicates 1 to 2 layers in FL-$Ti_3C_2T_x$ (the thickness of an individual MXene flake is reported to be 0.98 nm based on HRTEM study and DFT calculations).[15,16] The spikes in the thickness shown in the line scan of Fig. S2a† compared to the reported single-layered MXene thickness are likely due to the presence of surface adsorbents, such as water molecules trapped under the
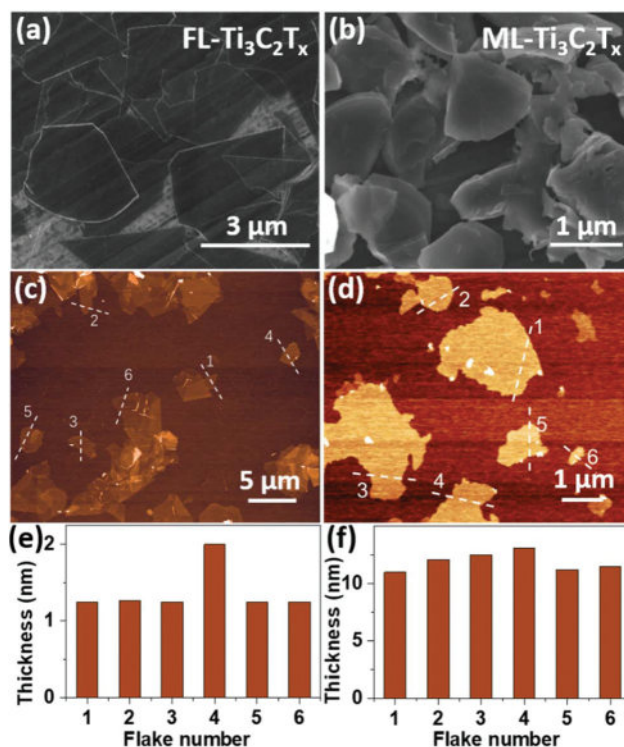

Fig. 1 FESEM images of (a) FL-$Ti_3C_2T_x$ and (b) ML-$Ti_3C_2T_x$; AFM images of (c) FL-$Ti_3C_2T_x$ and (d) ML-$Ti_3C_2T_x$ deposited on Si/SiO$_2$, and (e and f) statistical distribution of the flake thickness of individual flakes measured along the dashed lines in c and d.

FL-$Ti_3C_2T_x$ flake. In contrast, ML-$Ti_3C_2T_x$ in Fig. 1(d) shows a height of *ca.* 10 nm to ~13 nm (Fig. 1f and Fig. S2b†), which validates its multi-layered nature. The XPS analysis of FL-$Ti_3C_2T_x$ and ML-$Ti_3C_2T_x$ is discussed in Fig. S3, ESI.†

Next, we investigated the inherent electrochemistry of both ML-$Ti_3C_2T_x$ and FL-$Ti_3C_2T_x$ under anodic and cathodic cyclic voltammetry (CV) in the potential window of −1.8 to +1.8 V (electrolyte: pH 7 phosphate buffer solution, all the potentials stated in this paper are *versus* a Ag/AgCl reference electrode).
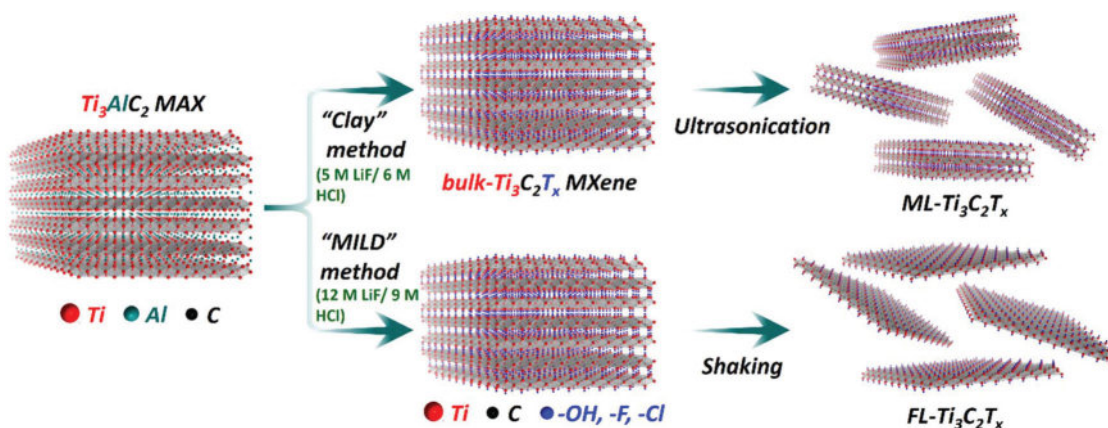
Scheme 1 Scheme representing the synthesis route to prepare bulk, ML– and FL-$Ti_3C_2T_x$ from the parent Ti_3AlC_2 MAX phase.

The electrode fabrication technique is discussed in the Experimental section. Fig. 2 shows the measured CVs in both anodic and cathodic directions. Three consecutive scans were recorded for each MXene electrode. The first anodic scan of FL-$Ti_3C_2T_x$ resulted in a prominent oxidation peak at +0.7 V with a shoulder peak overlapping at nearly 0.37 V (Fig. 2a). The cathodic CV scan indicates an oxidation peak at 0.43 V with a mild reduction peak at −1.1 V (Fig. 2b). For ML-$Ti_3C_2T_x$, the oxidation peak in the anodic scan occurs distinctly at 0.34 V with a mild reduction peak at −1.4 V (Fig. 2c), while the first scan towards a cathodic potential results in mild oxidation peaks at +0.3 V and a reduction peak at −1.1 V respectively (Fig. 2d). It is understood that the origin of the redox peaks in any voltammogram is from either the electrochemical reaction of redox moieties present in the electrode material itself or the redox active probe in the electrolyte. As the electrolyte is free from any redox-active probe, it is clear that the measured redox current is due to the redox reaction of $Ti_3C_2T_x$ itself. Also, it is observed that the reduction peak is less prominent during the anodic scan, which indicates that the initial oxidation makes the redox active moieties on $Ti_3C_2T_x$ flakes less prone to reduction. In parallel, the initial cathodic scan resulted in a less prominent oxidation peak compared to the initial anodic scan. CVs were also recorded for bulk-$Ti_3C_2T_x$ MXene (Fig. S4a and b†) and parent Ti_3AlC_2 MAX phases

(Fig. S4c and d†) under similar experimental conditions. Very similar CV features, but with a lower current were observed for bulk-$Ti_3C_2T_x$. However, interestingly, no prominent oxidation/reduction is observed for both scan directions in the parent Ti_3AlC_2 MAX phase, indicating the absence of redox active moieties.

A key feature observed in the above study is the complete disappearance of redox peaks in subsequent scans in both cathodic and anodic directions for all MXene electrodes, indicating the complete stabilization of the surface redox active moieties in the first scan itself. We may proclaim that the redox processes are largely chemically irreversible as the respective redox moieties were not re-oxidized/re-reduced in subsequent scans. Despite this, the inherent processes are highly dependent on the flake thickness of $Ti_3C_2T_x$, as evident from Fig. 2. In the anodic scan of FL-$Ti_3C_2T_x$ (Fig. 2a), the oxidation peak intensity is 1200 μA during the first scan, which falls to 220 and 35 μA for ML-$Ti_3C_2T_x$ and bulk-$Ti_3C_2T_x$, respectively (Fig. 2c and Fig. S4a†). The oxidation peak in the cathodic scan also exhibits a drop in the current intensity from 234 μA (for FL-$Ti_3C_2T_x$) in the initial scan to 67 and 35 μA for ML-$Ti_3C_2T_x$ and bulk-$Ti_3C_2T_x$, respectively (Fig. 2b and d, and Fig. S4b†). These changes in the current values are also replicated for other redox peaks in both cathodic and anodic sweeps.

The irreversible oxidation in the positive potential window in all MXene electrodes is deemed due to the anodization of surface Ti atoms, possibly at the defect sites and edges, which are more prone to oxidation. The reduction peak can be attributed to the removal of surface termination groups (mainly –OH, –O).[17,18] The absence of an oxidation peak at the MAX phase modified electrode, its appearance in bulk-$Ti_3C_2T_x$ and more prominent oxidation after slicing bulk-$Ti_3C_2T_x$ into ML-$Ti_3C_2T_x$ and FL-$Ti_3C_2T_x$ can be due to the introduction of surface defects in the synthesis process.[15] In addition, a large specific surface area in FL-$Ti_3C_2T_x$ could be the reason for the visibly larger redox current compared to those of ML- and bulk-$Ti_3C_2T_x$.

We also investigated the pH dependence of the redox peaks during the anodic scan of ML-$Ti_3C_2T_x$ at various pH values ranging from 2 to 12. Since the subsequent scans result in no further oxidation, only the first scans of each electrode were compared. All CVs and the variation of the oxidation peak potential (E_p) and peak current (I_p) with pH are shown in Fig. 2(e and f). The anodic peak at pH 7 appears at +0.39 V vs. Ag/AgCl, which progressively shifts toward lower values with a declined oxidation current as the pH decreases towards acidic levels. Surprisingly at pH 2, no oxidation is observed with a highly liberated oxygen evolution reaction (OER) current. In contrast, for alkaline pH, a shifted oxidation potential towards a more positive value is observed with progressive enhancement in the oxidation current. Hence the $Ti_3C_2T_x$ MXene is highly prone to oxidation in alkaline medium.

Since the anodic scan results in prominent oxidation and FL-$Ti_3C_2T_x$ liberates more oxidation current, we characterized FL-$Ti_3C_2T_x$ after conducting the anodic scan. The HRTEM and
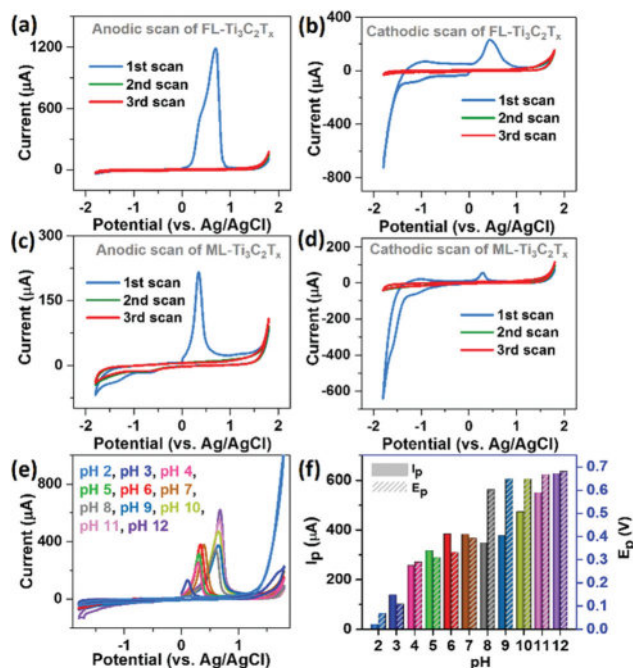

Fig. 2 Inherent electrochemical properties of $Ti_3C_2T_x$ MXene. Cyclic voltammograms showing anodic and cathodic scans of (a and b) FL-$Ti_3C_2T_x$ and (c and d) ML-$Ti_3C_2T_x$, (e) CVs of ML-$Ti_3C_2T_x$ during the anodic scan in PBS (0.1 M) at pH starting from 2 to 12. Conditions: Background electrolyte, PBS (0.1 M, pH 7.0); scan rate, 100 mV s^{-1}; (f) summary of peak potential (E_p) and peak current (I_p) at different pH of the electrolyte medium. The mass loading was maintained the same for all the modified electrodes to carry out a comparative analysis.
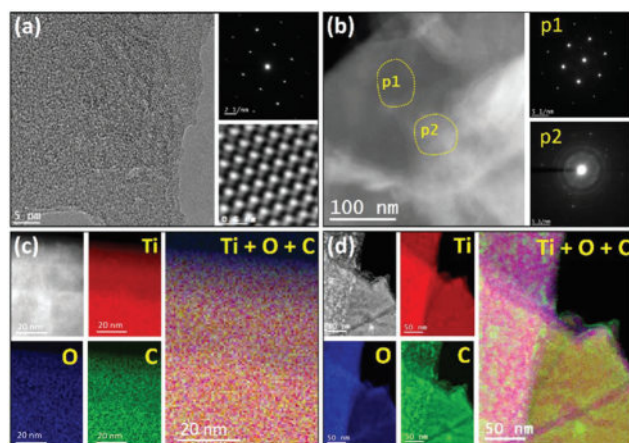
Fig. 3 HRTEM image of (a) FL-Ti$_3$C$_2$T$_x$ flakes; the inset shows SAED pattern (upper) and lattice resolved HRTEM image (lower) of FL-Ti$_3$C$_2$T$_x$; (b) STEM image of FL-Ti$_3$C$_2$T$_x$ resulting from the anodic scan; insets show the SAED pattern at selected areas p1 and p2, elemental mapping and mixed elemental mapping (c) before and (d) after the anodic scan.

STEM micrographs for FL-Ti$_3$C$_2$T$_x$ (Fig. 3a) depict the 2D layer structure with the hexagonal atomic arrangement (see the selected area electron diffraction (SAED) pattern in the upper inset and the HRTEM image in the lower inset).[16,19] In contrast, anodized FL-Ti$_3$C$_2$T$_x$ (Fig. 3b) depicts un-oxidized fragments (region p1) and a partially oxidized surface (region p2). This is supported by the corresponding SAED pattern, which

indicates the hexagonal phase of Ti$_3$C$_2$T$_x$ and diffraction rings of amorphous regions. Again, the elemental maps for FL-Ti$_3$C$_2$T$_x$ (Fig. 3c) confirm the composition and distribution of Ti, C, and O. The overlapped map indicates a homogeneous structural feature in FL-Ti$_3$C$_2$T$_x$. In contrast, the map for anodized FL-Ti$_3$C$_2$T$_x$ (Fig. 3d) displays oxygen-rich fragments, confirmed by a non-uniform structural feature on anodized FL-Ti$_3$C$_2$T$_x$.

The quantitative evaluation of the extent of oxidation after the anodic scan was done by X-ray photoelectron spectroscopy (XPS), shown in Fig. S5.† The deconvoluted Ti 2p spectra reveal different valence/charged states of Ti (listed in Table S1†).[20] The peak with a formal valence of 4$^+$ located at 458.5 eV corresponds to TiO$_2$. The peak located at 459.3 eV corresponds to TiO$_{2-x}$F$_x$. The concentrations of TiO$_2$ appear to be 3.9% and 4.32% before and after subjecting to the anodic scan, whereas the concentration of TiO$_{2-x}$F$_x$ changes from 6.6% to 15.5% (Fig. S5b, d and Table S1†). This confirms that the electrochemical anodic scan does not completely oxidize MXene, but rather makes it more stable by the introduction of oxidation debris on the Ti$_3$C$_2$T$_x$ surface.

To understand the trends in heterogeneous charge transfer kinetics in Ti$_3$C$_2$T$_x$ MXene, we conducted CVs using both inner- and outer-sphere electrochemical redox probes such as [Fe(CN)$_6$]$^{4-/3-}$ and [Ru(NH$_3$)$_6$]$^{3+/2+}$ respectively for both FL-Ti$_3$C$_2$T$_x$ (Fig. 4) and ML-Ti$_3$C$_2$T$_x$ (Fig. S6†). As reflected in Fig. 4a, for FL-Ti$_3$C$_2$T$_x$, the initial scan in the presence of [Fe(CN)$_6$]$^{4-/3-}$ resulted in a clear observation of the ferro/ferri-
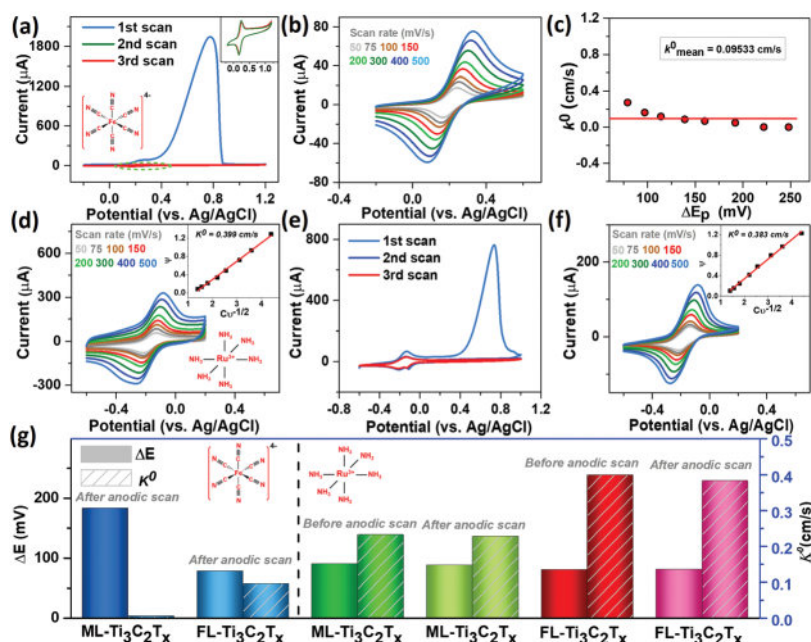

Fig. 4 Cyclic voltammograms of FL-Ti$_3$C$_2$T$_x$ MXene flakes recorded for 5 mM [Fe(CN)$_6$]$^{4-/3-}$ in 0.1 M KCl as the supporting electrolyte: (a) initial three consecutive scans at 50 mV s^{-1} scan rate and (b) CVs at varying scan rates from 50 to 500 mV s^{-1} after recording 1st three scans. CVs recorded for 5 mM [Ru(NH$_3$)$_6$]$^{3+/2+}$ in 0.1 M KCl as the supporting electrolyte at (d) scan rates from 50 to 500 mV s^{-1}; (e) three consecutive scans recorded at 50 mV s^{-1} scan rate after recording (d); (f) again at varying scan rates from 50 to 500 mV s^{-1}. Corresponding Klingler–Kochi and Nicholson analyses and calculated HET rate (k^0) are shown in (c) and insets of (d and f), (g) summary of peak-to-peak separations (ΔE) and HET rate (k^0) of ML-Ti$_3$C$_2$T$_x$ and FL-Ti$_3$C$_2$T$_x$ after and before the anodic scan for both inner and outer sphere redox couples: [Fe(CN)$_6$]$^{4-/3-}$ and [Ru(NH$_3$)$_6$]$^{3+/2+}$.

cyanide redox peaks (zoomed in insets) along with a predominant oxidation peak due to the inherent oxidation of $Ti_3C_2T_x$ MXene. But the successive scans resulted in only redox peaks corresponding to $[Fe(CN)_6]^{4-/3-}$. After recording three consecutive scans, we recorded CVs at different scan rates (Fig. 4b). In contrast, in the presence of the $[Ru(NH_3)_6]^{3+/2+}$ redox probe, the initial scans don't display any oxidation peak except the redox peaks of the probe (Fig. 4d). This validates the inherent electrochemistry of MXene that it undergoes irreversible oxidation in the positive potential window only. After recording the CVs at different scan rates, we again changed the potential range from −0.6 to 1 V, which resulted in the redox peaks corresponding to the $[Ru(NH_3)_6]^{3+/2+}$ redox probe along with the irreversible oxidation peak corresponding to MXene surface oxidation (Fig. 4e). Again, in sequence with our previous claims, the follow-up scans resulted in no oxidation of MXene and display only redox peaks of the probe. After recording three consecutive scans, we recorded CVs at different scan rates as shown in Fig. 4f. We employed both classical Nicholson method (limited to ΔE_p below 220 mV) and the method developed by Klingler and Kochi (when ΔE_p exceeds 220 mV) to calculate the heterogeneous charge transfer coefficient (k^0) (discussed briefly in the ESI†).[21–23] The calculated k^0 values and peak-to-peak separations (ΔE) are summarized in Fig. 4g. As observed, the k^0 value for $[Fe(CN)_6]^{4-/3-}$ increases on moving from ML-$Ti_3C_2T_x$ to FL-$Ti_3C_2T_x$, which agrees well with the literature on other 2D materials like graphene and TMDs (compared in Tables S2 and S3†).[24–34] It is seen that the k^0 value for $[Ru(NH_3)_6]^{3+/2+}$ does not vary much in going from ML-$Ti_3C_2T_x$ to FL-$Ti_3C_2T_x$ MXene or before and after the anodic scan. This could be due to the inert nature of the outer-sphere redox probe towards a number of layers and surface moieties (oxidation debris, functional groups).[30,35] This behavior highly piqued our curiosity to compare the charge transfer behavior of the MXene before and after the anodic scan. An in-depth analysis is desired to identify the role of the oxidation debris in charge transfer.

After examining the inherent electrochemistry and charge transfer studies of FL-$Ti_3C_2T_x$ and ML-$Ti_3C_2T_x$ flakes, we extended our investigation to the FL-$Ti_3C_2T_x$ MXene free-standing film electrode. Such study can reveal interesting insights into the stability of the MXene free-standing film electrode against irreversible oxidation in the positive potential window and justify our findings in favor of using it for biosensing and many analytical applications. The free-standing electrodes were prepared from FL-$Ti_3C_2T_x$ flakes and the electrode preparation scheme is discussed in the Materials and methods section. We performed surface, morphological and structural characterization of the FL-$Ti_3C_2T_x$ MXene free-standing film electrode before and after conducting the anodic scan. A digital photograph (Fig. 5a) shows an as-fabricated freestanding FL-$Ti_3C_2T_x$ MXene film. Fig. 5b–g show the top-view and cross-sectional FESEM micrographs of the free-standing film electrode before and after conducting the anodic scan. The insets of Fig. 5b and c show the digital images of the free-standing film electrode before and after conducting the anodic
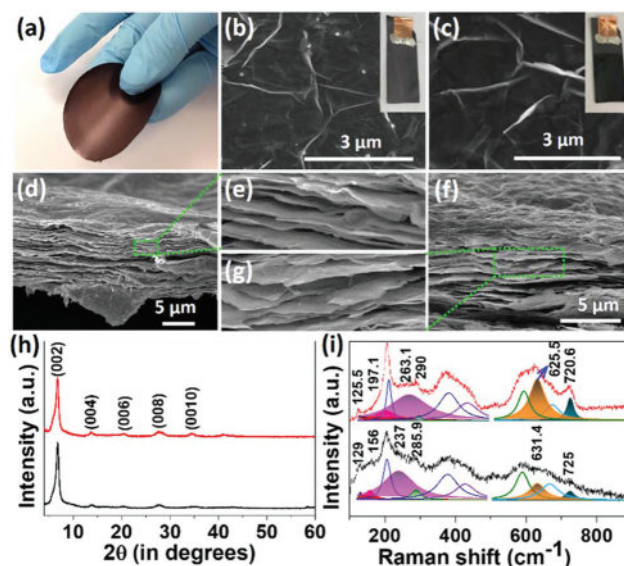

Fig. 5 (a) Digital photographs showing a flexible FL-$Ti_3C_2T_x$ MXene free-standing film. Top view FESEM image of the FL-$Ti_3C_2T_x$ MXene film electrode (b) before and (c) after anodic CV; insets: digital photograph of corresponding electrode design; cross-sectional FESEM image of the MXene free-standing electrode (d) before and (f) after recording anodic CV; projections (e and g) show the corresponding high resolution FESEM images, (h) X-ray diffractogram and (i) Raman spectra of the FL-$Ti_3C_2T_x$ MXene film electrode before (black plot) and after (red plot) anodic CV.

scan. As evinced, no structural incongruity is observed before and after recording anodic CV. Including this, the XRD analysis (Fig. 5h) of the free-standing film electrode suggests no obliteration in the structure and confirms that the oxidation debris formed on the MXene surface consists of very thin amorphous oxidized fragments, which is supported by our previous HRTEM and STEM mapping analyses. Fig. 5(i) represents the Raman spectra recorded on the FL-$Ti_3C_2T_x$ MXene free-standing film electrode before and after conducting anodic CV. The Raman peaks corresponding to different vibration modes of Ti–C, Ti–C–T_x are observed for the as prepared film electrode. Since the MXene is chemically etched and delaminated, usually it is terminated with –OH, –O and –F functionalities, which weakens the out-of-plane vibration of surface Ti_2 and strengthens the out-of-plane vibration of C atoms.[36,37] It is observed that the peak associated with doubly degenerated E_g modes at 156 cm^{-1} corresponding to in-plane vibrations of Ti_2 and C atoms in the as-prepared FL-$Ti_3C_2T_x$ film shifts to a lower wavenumber 125 cm^{-1} after the anodic scan, which indicates termination by surface –OH functional groups. Similarly, a shift toward a lower wavenumber and simultaneous strengthening of the peaks assigned to out-of-plane vibrations of C atoms in $Ti_3C_2O_2$ (631.4 and 725 cm^{-1}) are observed, which indicate the attachment of –O functionalities after the anodic scan.[38] Hence it is clearly understood that the anodic scan develops amorphous oxidized fragments over the $Ti_3C_2T_x$ MXene surface without any substantial alteration of properties,

indicating the stability of the MXene freestanding electrode for various applications.

Ti$_3$C$_2$T$_x$ is the most representative member of the MXene family, which has shown its novelty in many applications due to its unique physicochemical properties. However, its electrochemical behavior is highly dependent on many factors such as defects, surface terminations (–OH, –O, –F, *etc.*) and degree of delamination, which are altered vastly by its processing protocols that determine the quality of the 2D flakes produced.[39] This study is the first step toward understanding the fundamental inherent electrochemistry of Ti$_3$C$_2$T$_x$ MXenes with different flake thicknesses and open a wide window for its use as an electrode material for various electrochemical applications in an aqueous medium. Also, there are now close to 25 members of the MXene family with different transition metals, such as Nb, Mo, V, and so forth, which should be similarly investigated and explored to understand their potential use in different applications in an aqueous medium.[9]

Conclusions

In summary, we have studied the inherent electrochemistry of Ti$_3$C$_2$T$_x$ MXene and found that it undergoes irreversible oxidation in the positive potential window in an aqueous medium, which is due to Ti anodization. This effect is highly dependent on the flake thickness and pH of the electrolyte. Also, it is shown that few-layered Ti$_3$C$_2$T$_x$ exhibits faster electron transfer kinetics (k^0 = 0.09533 cm s^{-1}) with the Fe(CN)$_6^{4-/3-}$ redox mediator compared to multi-layered Ti$_3$C$_2$T$_x$ (k^0 = 0.00503 cm s^{-1}). In spite of this, no ample alteration of properties was observed even in the MXene free-standing film electrode in aqueous medium and positive potential window.

Experimental

Materials and methods

Materials. Potassium ferrocyanide [K$_4$[Fe(CN)$_6$], 99.9%], hexaaminruthenium(III) chloride [Ru(NH$_3$)$_6$Cl$_3$, 98%], and potassium chloride (KCl, 99%) were purchased from Sigma-Aldrich. Layered ternary carbide (Ti$_3$AlC$_2$) MAX phase powder was procured from Carbon-Ukraine Ltd (particle size < 40 μm). Dimethylformamide ((CH$_3$)$_2$NC(O)H, DMF) was purchased from Sigma Aldrich. Concentrated hydrochloric acid (HCl, technical grade, 35–38%) was procured from Fischer Scientific. Lithium fluoride (LiF, 98+%) was purchased from Alfa Aesar. Polypropylene (3501 coated PP) and cellulose nitrate (0.22 μm pore size) filter paper were procured from Celgard LLC, NC. Pt wire counter electrode, Ag/AgCl (1 M KCl) reference electrode and glassy carbon (GC) working electrode were purchased from CH Instruments, Texas, USA. PBS was purchased from Fisher Scientific-US. All the reagents were of analytical grade and were used as received. All stock solutions were prepared using deionized (DI) water (18.2 MΩ cm, Milli-Q Direct 8,

Merck Millipore, and Billerica, MA) without further purification.

Preparation of Ti$_3$C$_2$T$_x$ MXene. All chemicals were used as received without further purification. Ti$_3$C$_2$T$_x$ MXene was synthesized following the LiF/HCl clay method reported elsewhere.[14] The etching solution was prepared by adding 1.33 g of LiF to 20 ml 6 M HCl followed by stirring for 5 min. 2 g of Ti$_3$AlC$_2$ powder was slowly added to the etchant at 35 °C and stirred for 24 h. The acidic suspension was washed with deionized (DI) water until pH ≥ 6 *via* centrifugation at 3500 rpm (5 min per cycle) and decanting the supernatant after each cycle. The final product, with a small amount of water, was filtered using cellulose nitrate filter paper followed by drying under vacuum at 70 °C overnight and was referred to as bulk-Ti$_3$C$_2$T$_x$ MXene.

Preparation of 2D Ti$_3$C$_2$T$_x$ MXene flakes. The previously prepared clay was used to prepare ML-Ti$_3$C$_2$T$_x$ flakes. To obtain FL-Ti$_3$C$_2$T$_x$, we followed the minimum intensive layer delamination (MILD) technique.[13] The synthesis protocol is described as follows.

ML-Ti$_3$C$_2$T$_x$. To obtain a dispersion of ML-Ti$_3$C$_2$T$_x$ flakes, about 300 mg of freshly synthesized bulk-Ti$_3$C$_2$T$_x$ MXene powder was dispersed in 30 ml of DMF and stirred using a magnetic Teflon coated bar for 10 minutes at 500 rpm. The dispersion was sonicated for 30 minutes under ice bath conditions under Ar in order to prevent oxidation. After sonication, the suspension was centrifuged at 3500 rpm for 5 minutes and then decanted to separate the supernatant dispersion from sediment MXene particles. The supernatant suspension was named ML-MXene and was stored in a Teflon sealed glass vial by purging N$_2$ gas. The material concentration in the supernatant was calculated roughly by filtering a calculated amount of the supernatant by vacuum filtration, drying the filtrate under vacuum and finally measuring the weight difference of the filter paper and dried ML-MXene on the filter paper.

FL-Ti$_3$C$_2$T$_x$. FL-Ti$_3$C$_2$T$_x$ was prepared by the MILD technique. In brief, the etching solution was prepared by adding 1 g LiF to 20 ml 9 M HCl followed by stirring for 5 min. 1 g of Ti$_3$AlC$_2$ powder was slowly added to the MILD etchant at 35 °C and stirred for 24 h. The acidic suspension was washed with deionized (DI) water until pH 6 *via* centrifugation at 3500 rpm (5 min per cycle) and decanting the supernatant after each cycle. Around pH ≥ 6, the stable dark green supernatant of FL-Ti$_3$C$_2$T$_x$ was observed and then collected after 30 min centrifugation at 3500 rpm. The concentration of the FL-Ti$_3$C$_2$T$_x$ solution was measured by filtering specific amounts of the colloidal solution followed by drying under vacuum at 70 °C overnight and measuring the weight.

Preparation of free-standing Ti$_3$C$_2$T$_x$ MXene film electrode. An FL-Ti$_3$C$_2$T$_x$ free-standing film was prepared by vacuum filtration using polypropylene filter paper followed by drying under vacuum at 70 °C overnight. The free-standing film electrode was prepared by cutting a piece of required dimension and making contacts using conducting copper tape and silver paste. The fabricated electrode was used to perform an anodic

scan and further characterized to confirm the viability of the electrode for various applications.

Characterization methods

XRD patterns were collected using a Bruker diffractometer (D8 Advance) with Cu Kα radiation with scanning rates of 0.02° per step and 0.5 s/step in the 2θ angle range of 5°–50°. The morphology and microstructure of the samples were characterized by high-resolution field emission scanning electron microscopy (Nova Nano 630, FEI) and high-resolution transmission electron microscopy (Titan 80–300 kV). Cross-sectional SEM was employed to measure the thickness of free-standing MXene films. Raman spectroscopy measurements were carried out on the samples using a micro-Raman spectrometer (LabRAM Aramis, Horiba, Japan) equipped with a 473 nm wavelength cobalt blue laser and an Olympus ×50 objective lens. XPS studies were carried out in a Kratos Axis Ultra DLD spectrometer equipped with a monochromatic Al Kα X-ray source ($h\nu$ = 1486.6 eV) operating at 150 W, a multi-channel plate and a delay line detector under a vacuum of $\sim10^{-9}$ mbar. All spectra were recorded using an aperture slot of 110 μm × 110 μm. The survey and high-resolution spectra were collected at fixed analyzer pass energies of 160 and 20 eV, respectively. The spectral de-convolution was done using CASA XPS software.

Inherent electrochemistry studies on ML-Ti₃C₂Tₓ and FL-Ti₃C₂Tₓ. Fundamental electrochemical studies on MXene samples were performed in 0.1 M PBS of pH 7 as the background electrolyte. All the electrochemical measurements were performed using a CHI 608D workstation (Austin, USA). Cyclic voltammetry was used as the main technique to characterize the MXene modified electrodes. Prior to each new electrochemical measurement, the GCE was cleaned by polishing with a 0.05 μm alumina slurry on a polishing pad, thoroughly washed with deionized water and dried by purging N₂ gas. The Ti₃AlC₂ MAX phase, bulk-Ti₃C₂Tₓ, ML-Ti₃C₂Tₓ and FL-Ti₃C₂Tₓ MXene dispersion (1 mg ml⁻¹ concentration) were ultrasonicated for a period of 5 min to maintain the well-dispersed suspension. Aliquots of 2 μL of the suspension inks were dropcast on the GCE and were left to dry under a lamp with the N₂ flow. The above step was repeated 2 times in order to yield an electrode surface homogeneously modified with 4.0 μg film of the desired material. All cyclic voltammetry experiments were conducted at a scan rate of 100 mV s⁻¹. Both anodic and cathodic scans were started from 0 V, the potential at which no redox process is predicted to occur. In a typical anodic CV, the voltammetry scan began at 0 V and proceeded toward 1.8 V followed by a reverse sweep to −1.8 V and for the cathodic study, the first scan was toward −1.8 V followed by a reverse sweep to 1.8 V before returning to 0 V. All of the measurements were conducted under ambient conditions.

Heterogeneous electron transfer (HET) rate. The modified electrodes were tested for heterogeneous electron transfer (HET) studies using cyclic voltammetry at a scan rate from 50 to 500 mV s⁻¹ for both inner-sphere and outer sphere redox probes: 5 mM of K₄[Fe(CN)₆] and [Ru(NH₃)₆Cl₃] in KCl (0.1 M)

as the supporting electrolyte. The k^0 values were calculated from the Nicholson method and Klinger-Kochi methods. The roughness of the electrode was not factored into the calculation of k^0. The diffusion coefficients $D = 7.26 \times 10^{-6}$ cm² s⁻¹ and 8.43×10^{-6} cm² s⁻¹ were used to compute the k^0 values for $[Fe(CN)_6]^{4-/3-}$ and $[Ru(NH_3)_6]^{3+/2+}$ respectively.

Conflicts of interest

The authors declare no conflict of interest.

Acknowledgements

References

1 M. Naguib, M. Kurtoglu, V. Presser, J. Lu, J. Niu, M. Heon, L. Hultman, Y. Gogotsi and M. W. Barsoum, *Adv. Mater.*, 2011, **23**, 4248–4253.

2 M. Naguib, O. Mashtalir, J. Carle, V. Presser, J. Lu, L. Hultman, Y. Gogotsi and M. W. Barsoum, *ACS Nano*, 2012, **6**, 1322–1331.

3 M. Naguib, V. N. Mochalin, M. W. Barsoum and Y. Gogotsi, *Adv. Mater.*, 2014, **26**, 992–1005.

4 K. Maleski, V. N. Mochalin and Y. Gogotsi, *Chem. Mater.*, 2017, **29**, 1632–1640.

5 F. M. Römer, U. Wiedwald, T. Strusch, J. Halim, E. Mayerberger, M. W. Barsoum and M. Farle, *RSC Adv.*, 2017, **7**, 13097–13103.

6 Y. Peng, B. Akuzum, N. Kurra, M.-Q. Zhao, M. Alhabeb, B. Anasori, E. C. Kumbur, H. N. Alshareef, M.-D. Gerc and Y. Gogotsi, *Energy Environ. Sci.*, 2016, **9**, 2847–2854.

7 N. Kurra, B. Ahmed, Y. Gogotsi and H. N. Alshareef, *Adv. Energy Mater.*, 2016, **6**, 1601372.

8 H. Kim, B. Anasori, Y. Gogotsi and H. N. Alshareef, *Chem. Mater.*, 2017, **29**, 6472–6479.

9 B. Anasori, M. R. Lukatskaya and Y. Gogotsi, *Nat. Mater.*, 2017, **2**, 16098.

10 X. Wang, S. Kajiyama, H. Iinuma, E. Hosono, S. Oro, I. Moriguchi, M. Okubo and A. Yamada, *Nat. Commun.*, 2015, **6**, 6544.

11 K. Rasool, M. Helal, A. Ali, C. E. Ren, Y. Gogotsi and K. A. Mahmoud, *ACS Nano*, 2016, **10**, 3674–3684.

12 S. Kajiyama, L. Szabova, H. Iinuma, A. Sugahara, K. Gotoh, K. Sodeyama, Y. Tateyama, M. Okubo and A. Yamada, *Adv. Energy Mater.*, 2017, **7**, 1601873.

13 M. Ghidiu, M. R. Lukatskaya, M.-Q. Zhao, Y. Gogotsi and M. W. Barsoum, *Nature*, 2014, **516**, 78–81.

14 M. Alhabeb, K. Maleski, B. Anasori, P. Lelyukh, L. Clark, S. Sin and Y. Gogotsi, *Chem. Mater.*, 2017, **29**, 7633–7644.

15 X. Sang, Y. Xie, M.-W. Lin, M. Alhabeb, K. L. Van Aken, Y. Gogotsi, P. R. C. Kent, K. Xiao and R. R. Unocic, *ACS Nano*, 2016, **10**, 9193–9200.

16 X. Wang, X. Shen, Y. Gao, Z. Wang, R. Yu and L. Chen, *J. Am. Chem. Soc.*, 2015, **137**, 2715–2721.

17 M. E. Sibert, *J. Electrochem. Soc.*, 1963, **110**, 65–72.

18 C. J. Zhang, S. Pinilla, N. McEvoy, C. P. Cullen, B. Anasori, E. Long, S.-H. Park, A. S-Ascaso, A. Shmeliov, D. Krishnan, C. Morant, X. Liu, G. S. Duesberg, Y. Gogotsi and V. Nicolosi, *Chem. Mater.*, 2017, **29**, 4848–4856.

19 X. Li, X. Yin, M. Han, C. Song, X. Sun, H. Xu, L. Cheng and L. Zhang, *J. Mater. Chem. C*, 2017, **5**, 7621–7628.

20 J. Halim, K. M. Cook, M. Naguib, P. Eklund, Y. Gogotsi, J. Rosen and M. W. Barsoum, *Appl. Surf. Sci.*, 2016, **362**, 406–417.

21 R. S. Nicholson, *Anal. Chem.*, 1965, **37**, 1351–1355.

22 R. J. Kllngler and J. K. Kochl, *J. Phys. Chem.*, 1981, **85**, 1731–1741.

23 A. N. Patel, M. G. Collignon, M. A. O'Connell, W. O. Y. Hung, K. McKelvey, J. V. Macpherson and P. R. Unwin, *J. Am. Chem. Soc.*, 2012, **134**, 20117–20130.

24 T. J. Davies, R. R. Moore, C. E. Banks and R. G. Compton, *J. Electroanal. Chem.*, 2004, **574**, 123–152.

25 D. A. C. Brownson, S. A. Varey, F. Hussain, S. J. Haigh and C. E. Banks, *Nanoscale*, 2014, **6**, 1607–1621.

26 M. Velick, D. F. Bradley, A. J. Cooper, E. W. Hill, I. A. Kinloch, A. Mishchenko, K. S. Novoselov, H. V. Patten, P. S. Toth, A. T. Valota, S. D. Worrall and R. A. W. Dryfe, *ACS Nano*, 2014, **8**, 10089–10100.

27 K. Griffiths, C. Dale, J. Hedley, M. D. Kowal, R. B. Kaner and N. Keegan, *Nanoscale*, 2014, **6**, 13613–13622.

28 C. B. Navarro, Z. P. L. Laker, J. P. Rourke and N. R. Wilson, *Phys. Chem. Chem. Phys.*, 2015, **17**, 29628–29636.

29 E. P. Randviir, D. A. C. Brownson, M. G. Mingot, D. K. Kampouris, J. Iniesta and C. E. Banks, *Nanoscale*, 2012, **4**, 6470–6480.

30 P. Nayak, N. Kurra, C. Xia and H. N. Alshareef, *Adv. Electron. Mater.*, 2016, **2**, 1600185.

31 A. Yong, S. Eng, A. Ambrosi, Z. Sofer, P. Šimek and M. Pumera, *ACS Nano*, 2014, **8**, 12185–12198.

32 X. Chia, A. Ambrosi, Z. Sofer, J. Luxa, D. Sedmidubský and M. Pumera, *ACS Nano*, 2016, **10**, 112–123.

33 X. Chia, Z. Sofer, J. Luxa and M. Pumera, *ACS Appl. Mater. Interfaces*, 2017, **9**, 25587–25599.

34 X. Chia, A. Ambrosi, D. Sedmidubsky, Z. Sofer and M. Pumera, *Chem. – Eur. J.*, 2014, **20**, 17426–11743.

35 P. Nayak, B. Anbarasan and S. Ramaprabhu, *J. Phys. Chem. C*, 2013, **117**, 13202–13209.

36 T. Hu, J. Wang, H. Zhang, Z. Li, M. Hu and X. Wang, *Phys. Chem. Chem. Phys.*, 2015, **17**, 9997–10003.

37 M. Hu, Z. Li, T. Hu, S. Zhu, C. Zhang and X. Wang, *ACS Nano*, 2016, **10**, 11344–11350.

38 M. Naguib, O. Mashtalir, M. R. Lukatskaya, B. Dyatkin, C. Zhang, V. Presser, Y. Gogotsi and M. W. Barsoum, *Chem. Commun.*, 2014, **50**, 7420–7423.

39 M. D. Levi, M. R. Lukatskay, S. Sigalov, M. Beidaghi, N. Shpigel, L. Daikhin, D. Aurbach, M. W. Barsoum and Y. Gogotsi, *Adv. Energy Mater.*, 2015, **5**, 1400815.